Recuperated solar-dish Brayton cycle using turbocharger and short-term thermal storage

Willem G. Le Roux[1*]

Adriano Sciacovelli[2]

[1] Department of Mechanical and Aeronautical Engineering, University of Pretoria,
Private Bag X20, Hatfield, Pretoria, 0028, South Africa

[2] School of Chemical Engineering, University of Birmingham, UK

*Corresponding author: willem.leroux@up.ac.za

Abstract

A recuperated solar-dish Brayton cycle with an off-the-shelf turbocharger as micro-turbine is investigated for potential low-cost power generation. Integrated phase-change thermal storage in the solar receiver can be used to improve the power stability and performance of the cycle; however, the phase-change temperature affects the solar conversion efficiency. In this paper, three different off-the-shelf turbochargers and various recuperator geometries are considered so that the maximum thermal efficiency of the cycle can be found for a fixed receiver geometry at different solar receiver temperatures. Metallic phase-change material of high conductivity is proposed as thermal storage material which is placed around a coiled tube in an open-cavity tubular solar receiver. An analytical model is presented to determine the thermal efficiency of the cycle for different solar receiver temperatures. Results show that maximum thermal efficiencies of 20.2% to 34.2% can be achieved at receiver temperatures of between 900 K and 1200 K, and that solar conversion efficiencies of 13.5% to 21% (11% to 17% when dish reflectivity and intercept factor are both assumed 90%) can be achieved. High solar conversion efficiencies require a large solar input power which would require a more expensive solar dish. A map is therefore provided for each turbocharger which shows the expected solar input power for the shaft power generated at different solar receiver temperatures. Overall, the results show that an open-cavity tubular solar receiver with metallic phase-change thermal storage material can be used together with an off-the-shelf turbocharger for power generation in a solar-dish Brayton cycle.

Keywords

Brayton cycle; turbocharger; solar-dish; micro-turbine; phase-change material; recuperator

Acknowledgements

This work is based on the research supported by the Royal Society of the United Kingdom (Newton Mobility Grant: NMG\R2\170082), the National Research Foundation (NRF) of South Africa (Grant Number 109311), the Technology Innovation Agency of South Africa (TIA) and the University of Pretoria's Research and Development Plan (RDP).

Nomenclature

A	Area, m^2
a	Aperture dimension of solar receiver, m
a	Width of recuperator channel, m
b	Height of recuperator channel, m
BSR	Blade speed ratio
c_p	Constant-pressure specific heat, J/kgK
D	Diameter, m
d	Receiver tube diameter, m
f	Friction factor
Gr	Grashof number
H	Total height of recuperator, m
h	Specific enthalpy, J/kg
h	Heat transfer coefficient, W/m^2K
K	Loss coefficient
k	Gas constant
k	Thermal conductivity, W/mK
L	Length, m
L_f	Latent heat of fusion, J/kg
MT	Micro-turbine number
$\dot{m}$	System mass flow rate, kg/s
N	Speed of micro-turbine shaft, rpm
n	Number of flow channels in parallel

NTU	Number of transfer units
Nu	Nusselt number
P	Pressure, Pa
Pr	Prandtl number
R	Gas constant, J/kgK
r	Pressure ratio
Re	Reynolds number
$\dot{Q}$	Heat transfer rate, W
$\dot{Q}_{loss}$	Heat loss rate, W
$\dot{Q}_{net}$	Net heat transfer rate, W
$\dot{Q}*$	Solar power available at the receiver cavity, W
$\dot{S}_{gen}$	Rate of entropy generation, W/K
t	Thickness, m
t_{PC}	Phase-change time, s
T	Temperature, K
*T**	Apparent temperature of the sun as an exergy source, K
U	Overall heat transfer coefficient, W/m^2K
V	Velocity, m/s
V_{PCM}	Volume of phase-change material, m^3
w	Wind factor
$\dot{W}$	Power, W
Z	Height, m

Greek Letters

ε	Emissivity of receiver cavity walls
η	Efficiency
θ	Angle of cavity axis with the horizontal, degrees
ρ	Density, kg/m^3
σ	Stefan-Boltzmann constant, W/m^2K

Subscripts

0	Zero-pressure (for c_p)
1-11	Refer to Fig. 1
	Aperture
ave	Average
c	Cold side
c	Compressor
cav	Cavity
CF	Corrected flow
cond	Conduction
conv	Convection
e	Exit
eff	Effective
h	Hot side
i	Inlet
in	At the inlet
ins	Insulation
int	Internal
L	Based on *L*
liquid	Liquid
max	Maximum
net	Net
opt	Optimum
optical	Optical
out	On the outside of the insulation
PC	Phase change
PCM	Phase-change material
rad	Radiation
rec	Receiver
refl	Reflectivity
reg	Recuperator

s	Surface
solar	Solar
solid	Solid
t	Turbine
th	Thermal
wall	Cavity wall
∞	Environment

1. Introduction

Small-scale solar power generation systems can provide electricity to small communities that do not have access to the national grid, as is typically found in southern Africa (Fluri et al., 2009). Small-scale systems have an advantage in terms of cost because of large-scale manufacturing possibilities. Power generation using a solar dish is often associated with the Stirling engine. Dish-Stirling engines are usually sized for electrical output of 3 to 30 kW (Andraka, 2014). A solar dish can also be applied as heat source for power generation using a Rankine cycle (Loni et al., 2018) or a Brayton cycle (Chen et al., 2007; Coventry and Andraka, 2017). Experimental testing by NASA, of a 10 kWe closed Brayton cycle intended for a solar dish, showed that the cycle had high reliability and efficiencies of above 30% at turbine inlet temperatures of between 1033 K and 1144 K (Pietsch and Brandes, 1989). Successful on-sun dish-Brayton demonstrations were performed in 1984 by Sanders Associates and in 2011 by Brayton Energy and Southwest Solar Technologies according to Coventry and Andraka (2017). According to Gavagnin et al. (2018), one of the most recent attempts to demonstrate a dish-Brayton cycle is the OMSoP project (Lanchi et al., 2015). The recuperated solar Brayton cycle has been tested on a larger scale, using a heliostat field and solar tower, producing 24 kW of electricity at an efficiency of 11.76% and a speed of 96 000 rpm (Dickey, 2011). Korzynietz et al. (2016) tested a megawatt-scale gas turbine hybrid with a tubular solar receiver without a recuperator. More than 1000 operation hours were achieved.

A recuperated solar-dish Brayton cycle with short-term thermal storage in the solar receiver is shown in Fig. 1. The proposed cycle uses air as working fluid in an open cycle. Air enters the cycle at the radial compressor powered by the turbine, which also produces shaft power for an electric load rotating at the same speed. According to Willis and Scott (2000), the configuration is simple and robust and is easy to maintain. The air is heated by thermal storage material in the solar receiver heated by concentrated solar power which is absorbed at the inner cavity walls of the solar receiver. A gas combustion chamber between the solar receiver and turbine can be used to develop a hybrid system for full-time operation (McDonald and Rodgers, 2002; Nelson et al., 2018). In the recuperator the air is preheated by hot exhaust air from the turbine before it enters the receiver. The recuperator allows for higher cycle efficiencies and operation at lower pressure ratios (Shah, 2005; Malali et al., 2017). The hot exhaust air leaving the cycle after the

recuperator can be used for cogeneration which increases the energy utilisation factor of the system (Le Roux, 2018). The accuracy of the solar dish and its tracking system as well as the size of the solar dish are important considerations which can significantly influence the total cost of the solar-dish Brayton cycle setup.

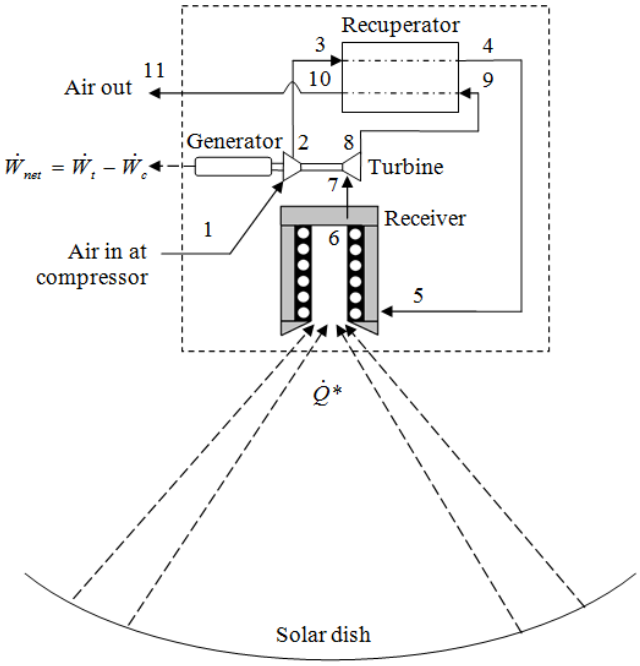

Fig. 1 Recuperated solar-dish Brayton cycle with integrated thermal storage.

To minimize costs, off-the-shelf turbochargers can be used as turbomachinery in a recuperated Brayton cycle, as was done by Visser et al. (2011) in the development of a 3 kW recuperated microturbine which has been commercialised for micro CHP applications. Coupling of a commercial turbocharger shaft to a high-speed generator requires a flexible coupling attached to the compressor inlet (Shiraishi and Ono, 2007) or an in-line, bolt-on housing (Carpenter et al., 2018). Turbochargers are available in many different sizes and at low cost because of large production volumes in the vehicle industry. Consequently, the solar-dish Brayton cycle has a cost advantage (Mills, 2004). It has therefore been proposed that an off-the-shelf turbocharger can be used as the micro-turbine for a recuperated solar-dish Brayton cycle (Le Roux et al., 2014b). Garrett (2014) for example, produces a variety of turbochargers in high production quantities. The maximum inlet temperatures of these off-the-shelf turbochargers are about 1223 K (Garrett, 2014; Shah, 2005) and 1323 K intermittently. It is expected that the

development and commercialisation of electrically-assisted turbochargers as well as micro-turbine range-extenders for electric vehicles will further increase the solar-dish Brayton cycle's advantage in terms of cost in the future.

Thermal storage systems can also be coupled to a solar Brayton cycle. Most Brayton cycles require a minimum temperature of 753 K to sustain itself (Stine and Harrigan, 1985). Thermal storage systems can allow the system to operate when the sun has set (which is also when there is a peak in electricity demand) or to balance out sudden fluctuations in the solar radiation due to clouds (Giovannelli et al., 2017). Storage such as lithium fluoride (Cameron et al., 1972; Asselman, 1976), packed rock beds (Allen, 2010; Ozturk et al., 2019), and encapsulated sodium sulphate (Klein, 2016) have been investigated. Phase-change materials can be used to provide a stable turbine inlet temperature; however, materials such as salt composites and inorganic salts have limited applications because of corrosion issues and large volume changes during melting, while most phase-change materials have a low thermal conductivity of around 0.5 W/mK (Liu et al., 2012). Metallic phase-change materials can be more advantageous in terms of achieving a constant turbine inlet temperature because of their higher thermal conductivities (Liu et al., 2012). Bashir et al. (2019) have investigated the use of Mg-Si as a metallic phase-change material integrated into a solar receiver for short-term thermal energy storage (30 minutes). Various metal and metal alloy phase-change materials (over a wide temperature range) are listed by Khare et al. (2012), Cárdenas and León (2013), Liu et al. (2012) and Cárdenas and León (2013). At Sandia National Laboratories, Andraka et al. (2015) have investigated the use of metallic phase-change materials with melting temperatures of between 1023 K and 1073 K specifically for solar dish-Stirling engines. Significant wall loss was observed in the containment alloys (316L Stainless Steel, In625 and H230) due to severe intermetallic diffusion of the investigated phase-change materials (Ca-Si and Cu-Mg-Si), mainly due to silicon and copper. Further research by Withey et al. (2016) found that a plasma sprayed Al_2O_3 protective coating (on H230) performed well to prevent this phenomenon. Yan and Fan (2001) also recommended ceramic coatings for steel in the containment of molten aluminium, since nickel dissolves in liquid aluminium. Al-Si has been proposed as an alternative phase-change material (Andraka et al., 2012) and also as a coating for stainless steel (Fu et al., 2017), which could be used as containment material.

According to Harris and Lenz (1983), overall solar collector efficiencies of 60-70% can be achieved with advanced systems using open-cavity receivers operating in the range of 773-1173 K (Harris and Lenz, 1983). Wang et al. (2015) experimentally tested a coiled tube solar receiver on a 56.8 m^2 solar dish and found an average efficiency of 60%. According to Wang et al. (2015), a coiled tube receiver has an advantage in terms of cost and easy installation. The receiver coil design also assists with the reduction of mechanical stresses due to thermal expansion (Heller et al., 2006). Numerous high-temperature solar receivers with higher efficiencies have been documented in the literature; however, these solar receivers are typically not optimised for performance in a recuperated Brayton cycle with turbocharger as micro-turbine with typical pressure ratios of 1.3-2.5; therefore Le Roux (2015) applied the method of total entropy generation minimisation (optimisation of the global performance) according to Bejan (2006) on the geometries of a low-cost open-cavity tubular receiver and plate-type recuperator. For a low-cost 4.8-m-diameter solar dish, it was found that open-cavity tubular receiver efficiencies of between 45% and 70% can be achieved with typical turbocharger mass flow rates of between 0.06 kg/s and 0.08 kg/s and receiver air inlet temperatures of between 900 K and 1070 K (Le Roux et al., 2014a). With the use of SolTrace, an optimum aperture length of a = 0.25 m and inner tube diameter of d = 0.0833 m was identified (see Fig. 2) for a 4.8-m-diameter solar dish with 45° rim angle, 1° tracking error and 10 mrad optical error (low-cost solar dish and tracking). With the use of Flownex and SolTrace, Le Roux and Meyer (2016) showed that, for a fixed aperture size and turbocharger, a smaller tube diameter for the open-cavity tubular receiver will decrease the output power of the solar-dish Brayton cycle.

Fig. 2 An open-cavity tubular solar receiver for an experimental setup.

In this paper, an open-cavity tubular solar receiver integrated with metallic phase-change material and coupled to a recuperated solar-dish Brayton cycle using an off-the-shelf turbocharger is considered. A metallic phase-change material of high conductivity is proposed to be placed around the receiver tube for integrated short-term thermal storage at the phase-change temperature. Different recuperator dimensions, phase-change temperatures and turbocharger operating points are considered in such a way that the maximum thermal efficiency of the cycle, and consequently the minimum required dish size for steady-state operation at the phase-change temperature, can be determined. Performance maps are shown which allows for the assessment of the cycle in terms of cost, power output, pressure ratio and phase-change temperature.

2. Methodology

The dimensions of the open-cavity tubular solar receiver stay constant in the analysis. The receiver surface temperature, chosen turbocharger and turbocharger operating point are parameters in the study, while the recuperator dimensions are variables. The required solar power input for steady-state operation at the solar receiver phase-change temperature, $\dot{Q}*$, is determined by calculation of $\dot{Q}_{net}$ and $\dot{Q}_{loss}$ (where $\dot{Q}* = \dot{Q}_{net} + \dot{Q}_{loss}$). $\dot{Q}*$ is a representation of the required solar dish size and dish accuracy, which in turn is a representation of the solar dish cost. This means that, for a larger solar power input, a larger solar dish with more precise solar optics would be required, which would also be more expensive.

2.1. Solar receiver

A compact high-temperature high-conductivity phase-change thermal storage material, as suggested by Giovannelli et al. (2017) and Bashir et al. (2019), is housed inside the solar receiver structure and around the open-cavity coiled tubular solar receiver (see Fig. 3) which was optimised for a recuperated solar-dish Brayton cycle using a turbocharger (Le Roux et al., 2014a) (see Fig. 2). Table 1 shows the dimensions of the receiver which are assumed constant in the analysis.

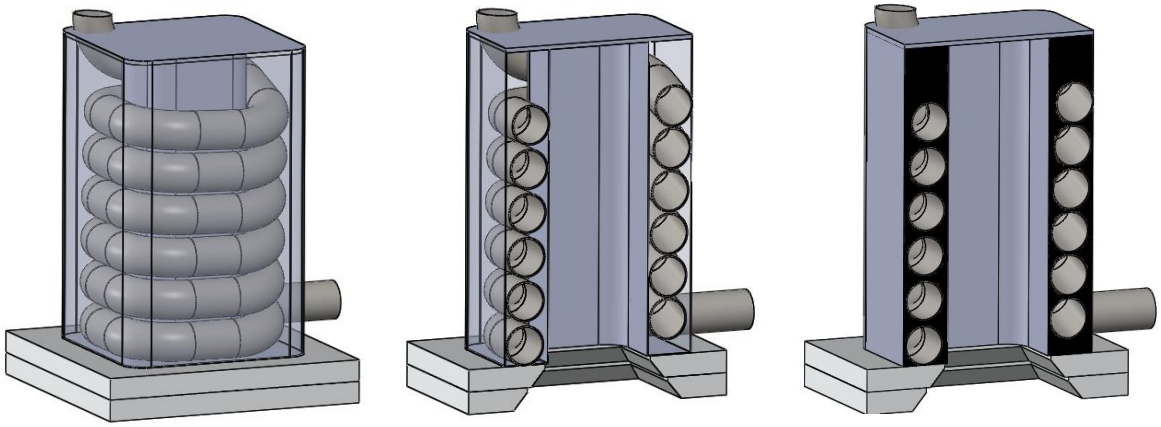

Fig. 3 The open-cavity tubular receiver (uninsulated) is shown without phase-change material (left, middle) and with phase-change material (right). The section views (middle, right) show the receiver aperture and open cavity.

Table 1 Open-cavity tubular receiver dimensions which stay constant in the analysis.

Constant	**Value**
Tube diameter, d (m)	0.0833
Aperture area, $a \times a$ (m^2)	$0.25 \times 0.25 = 0.0625$
Number of coils	6
Tube length (m)	8
Emissivity of receiver cavity, ε_{wall}	0.7
Insulation thickness, t_{ins} (m)	0.1
Insulation conductivity, k_{ins} (W/mK)	0.06-0.09 (900-1200 K) (Harris and Lenz, 1983)
Wind speed (m/s)	2.5
Wind factor, w	2
Average elevation angle, θ	45°
Ambient temperature (K)	300
Ambient pressure (kPa)	86

Solar beam irradiance is reflected from the solar dish and is absorbed at the receiver inner cavity wall. The inner cavity wall transfers heat to the metallic phase-change storage material (shown in black). The phase-change material stores heat but also transfers heat to the air which flows

through the tubular coil ($\dot{Q}_{net}$). The solar receiver (shown in Fig. 2) is modelled as a constant-surface-temperature tube. It is assumed that the tube surface temperature, T_s, is equal to the phase-change temperature of the metallic phase-change material. For steady-state operation, the exit temperature of the receiver is determined with Equation (1) and the net heat transfer rate with Equation (2).

$$T_e = T_s - (T_s - T_i)e^{-h_{rec}A_s/\dot{m}c_p} \tag{1}$$

$$\dot{Q}_{net} = h_{rec}A_s \frac{(T_i - T_e)}{\ln[(T_s - T_e)/(T_s - T_i)]} \tag{2}$$

The inner heat transfer coefficient is found by determining the Nusselt number using the Dittus–Boelter equation as shown in Equation (3). The pressure drop through the receiver tube is determined as shown in Equation (4).

$$h_{rec} = \frac{kNu}{d} = \frac{0.023k\,\mathrm{Re}^{0.8}\,\mathrm{Pr}^{0.4}}{d} \tag{3}$$

$$\Delta P = \frac{8\dot{m}^2}{\rho\pi^2 d^4}\left(f\frac{L}{d} + \sum_y K_y\right) \tag{4}$$

At steady state, the receiver operates at the phase-change temperature and the required solar power at the cavity walls is found with Equation (5). The solar power available at the cavity walls depends on the solar concentrator's shape, diameter, rim angle, reflectivity and optical error as well as tracking error and receiver alignment, which are not modelled in this analysis.

$$\dot{Q}^* = \dot{Q}_{loss,cond} + \dot{Q}_{loss,conv} + \dot{Q}_{loss,rad} + \dot{Q}_{net} \tag{5}$$

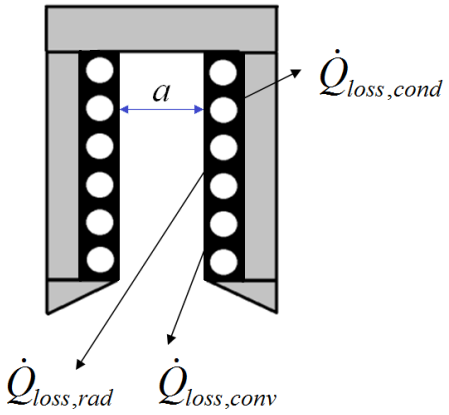

Fig. 4 A section view of the insulated open-cavity solar receiver showing heat loss (phase-change metal storage material shown in black).

Figure 4 shows a schematic of the heat losses from the insulated open-cavity receiver. The receiver has an aperture area of a^2. The heat loss rate due to conduction is calculated according to Le Roux et al. (2014a) as a function of the phase-change temperature. The radiation heat loss rate from the aperture is determined using Equation (6) and the effective emissivity with Equation (7) according to Jilte et al. (2013).

$$\dot{Q}_{loss,rad} = \varepsilon_{eff} A_{ap} \sigma \left(T_s^4 - T_\infty^4 \right) \tag{6}$$

$$\varepsilon_{eff} = \frac{1}{1 + \left(\frac{1 - \varepsilon_{wall}}{\varepsilon_{wall}} \right) \frac{A_{ap}}{A_{wall}}} \tag{7}$$

According to McDonald (1995), the heat losses can be calculated using the Koenig and Marvin model as was presented by Harris and Lenz (1983). For the open-cavity receiver, the convection heat loss rate is found using Equation (8) where h_{cav} is determined according to Harris and Lenz (1983) for $0 \leq \theta \leq 45°$,

$$\dot{Q}_{loss,conv} = w h_{cav} A_{wall} \left(T_s - T_\infty \right), \tag{8}$$

$$h_{cav} = Nu_{cav} k / L_{cav} = 0.52\left(\cos^{3.2}\theta\right)\left(Gr_L \,\mathrm{Pr}\right)^{1/4} k / L_{cav} \tag{9}$$

Note that L_{cav} is the mean inner cavity radius multiplied with $\sqrt{2}$ (Harris and Lenz, 1983) and therefore $L_{cav} = \sqrt{2a^2/\pi}$.

2.2 Recuperator

A plate-type counterflow recuperator is considered (Le Roux et al., 2014b) with aspect ratio of *a*/*b* (see Fig. 5). The pressure drop is calculated with Equation (10), where *f* is a function of the aspect ratio of a single flow channel as well as the Reynolds number. Table 2 shows the recuperator constants which are used in the analysis.

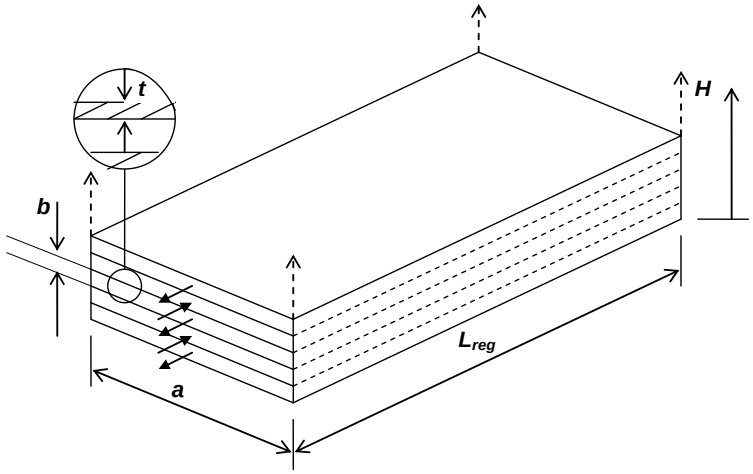

Fig. 5 Recuperator geometry (Le Roux et al., 2014b)

Table 2 Recuperator constants used in the analysis.

Constant	**Value**
Recuperator plate thickness, *t* (mm)	0.5
Conductivity of stainless steel (W/mK)	18.3 (600 K) (Çengel, 2006)
Recuperator insulation thickness, t_{ins} (m)	0.05
Recuperator insulation conductivity, k_{ins} (W/mK)	0.18
Recuperator outer convection heat transfer coefficient, h_{out} (W/m^{2}K)	25

$$\Delta P = \frac{fL_{reg}\left(\dot{m}/n\right)^2\left(a+b\right)}{4\rho\left(ab\right)^3} \tag{10}$$

The overall heat transfer coefficient, *U*, is determined by finding the forced convection heat transfer coefficients of a hot side channel, h_h, and a cold side channel, h_c. The convection heat transfer coefficient depends on the Reynolds number, aspect ratio and average temperature. The effectiveness is calculated using an *ε-NTU* method in which heat loss is included (Nellis and Pfotenhauer, 2005). The number of transfer units is determined with Equation (11). The heat loss from the recuperator channels (hot and cold) is determined according to Le Roux et al. (2014b). The total mass of the plates is limited to 500 kg in this study.

$$NTU_h = \frac{UaL_{reg}\left(2n-1\right)}{\dot{m}_h c_{p0,h}} \tag{11}$$

2.3 Turbine and compressor

A commercial off-the-shelf turbocharger (Garrett, 2014) is considered as micro-turbine for the recuperated solar-dish Brayton cycle. The turbine pressure ratio (r_t) is used as parameter in the analysis. The typical operating conditions of the turbocharger's turbine are found from the turbine map, where the pressure ratio is given as a function of the corrected mass flow rate. According to Garrett (2014), the actual mass flow rate is found using Equation (12), where the unit of P_7 is pounds per square inch and the unit of T_7 is degrees Fahrenheit.

$$\dot{m}_t = \frac{\dot{m}_{tCF} \times P_7 / 14.7}{\sqrt{\left(T_7 + 460\right)/519}} \tag{12}$$

The turbine efficiency is determined by finding the blade speed ratio (Westin, 2005; Batteh and Newman, 2008; Wahlström and Eriksson, 2011):

$$BSR = \frac{\frac{2\pi N}{60}\left(\frac{D_t}{2}\right)}{\left[2h_{in}\left(1-r_t^{\frac{1-k}{k}}\right)\right]^{1/2}}. \tag{13}$$

As shown in Equation (14), the blade speed ratio can be used to model the turbine efficiency with the use of a parabolic function (Wahlström and Eriksson, 2011). The maximum turbine efficiency is available from the turbine map and are in line with typical values for automotive applications of $\eta_{t,\max} \approx 0.65\text{-}0.75$ (Guzzella and Onder, 2010).

$$\eta_t = \eta_{t,\max}\left(1-\left(\frac{BSR-0.6}{0.6}\right)^2\right) \tag{14}$$

With the use of MATLAB, the shaft speed and isentropic compressor efficiency are determined by interpolation from a compressor map, using the compressor pressure ratio and the corrected mass flow rate (Garrett, 2014). To prevent flow surge and choking, the compressor is only allowed to operate within the range of its compressor map. According to Garrett (2014), the corrected compressor mass flow rate is found with Equation (15), where the units of P_1 and T_1 are pounds per square inch and degrees Fahrenheit, respectively. It is assumed that $\dot{m}_t = \dot{m}_c$.

$$\dot{m}_{cCF} = \frac{\dot{m}_c \times \sqrt{(T_1+460)/545}}{P_1/13.95} \tag{15}$$

2.4 Power output

For each component in the recuperated solar-dish Brayton cycle, a compromise must be made between heat transfer and pressure drop. Components are therefore optimised to reach a common goal, which is to maximise the cycle's thermal efficiency. Using MATLAB, the maximum thermal efficiency is evaluated for different phase-change temperatures in the receiver, while considering three different turbochargers, a number of differently sized recuperators (see Table 3) and a fixed receiver geometry (see Table 1).

Table 3 Recuperated solar-dish Brayton cycle parameters and variables.

Parameter	**Range**
Receiver phase-change temperature, T_s (K)	900-1200
Turbocharger number, *MT*	1-3
Turbine pressure ratio, r_t	According to turbine map of turbocharger
Variables	
Width of recuperator channel, *a* (mm)	150-450
Recuperator channel height, *b* (mm)	1.5-4.5
Length of recuperator, L_{reg} (m)	1.5-4.5
Recuperator number of parallel flow channels, *n*	15-45

The turbine pressure ratio (r_t) is used as parameter as was suggested by Lidsky et al. (1991), Wilson and Korakianitis (1998) as well as Snyman (2009). The turbine mass flow rate is coupled to the turbine pressure ratio according to the turbine map. The actual turbine mass flow rate is a function of the turbine inlet temperature and pressure and is found via iteration using Equation (12). The three off-the-shelf turbochargers (*MT*) which are considered are the *GT1241*, *GT2052* and *GT2860RS* from Garrett (2014). The *GT1241* is the smallest in the Garrett range. Four different receiver tube surface temperatures (T_s = 900 K, 1000 K, 1100 K and 1200 K) are investigated, where it is assumed that the receiver tube surface temperature is equal to the phase-change temperature of the metallic phase-change material.

The MATLAB program has the following stucture:

For *MT* = 1:1:3,

For T_s = 900:100:1200,

For each turbine pressure ratio (r_t) in the operating range of the turbine,

For each recuperator design (625 different combinations of *a*, *b*, L_{reg} and *n*),

- Find $\dot{W}_{net}$ and η_{th} of the cycle.

- Find required $\dot{Q}^*$ for steady-state operation at the phase-change temperature.

Heat losses and pressure losses in tubes connecting components are assumed to be negligible (the components are close to each other). The recuperator effectiveness as well as the isentropic efficiencies of the turbine and compressor is used to find the temperatures and pressures in the cycle by iteration. Note that $P_1 = P_{10}$ (see Fig. 1). By doing an exergy analysis for the recuperated solar-dish Brayton cycle and assuming $V_1 = V_{11}$ and $Z_1 = Z_{11}$, the net output power is shown in Equation (16) (Le Roux, 2015). The total entropy generation rate is shown in Equation (17) in terms of the pressures and temperatures of the cycle (see Fig. 1).

$$\dot{W}_{net} = -T_\infty \dot{S}_{gen,\text{int}} + \left(1 - \frac{T_\infty}{T^*}\right)\dot{Q}^* + \dot{m}c_{p0}\left(T_1 - T_{11}\right) - \dot{m}T_\infty c_{p0} \ln\left(\frac{T_1}{T_{11}}\right) \tag{16}$$

$$\begin{aligned}\dot{S}_{gen,\text{int}} = &\left[-\dot{m}c_{p0}\ln\left(T_1/T_2\right) + \dot{m}R\ln\left(P_1/P_2\right)\right]_{compressor} \\ &+ \left[\dot{m}c_{p0}\ln\left[\frac{T_{10}T_4}{T_9T_3}\left(\frac{P_{10}P_4}{P_9P_3}\right)^{-R/c_{p0}}\right] + \dot{Q}_{loss,reg}/T_\infty\right]_{recuperator} \\ &+ \left[-\frac{\dot{Q}^*}{T^*} + \frac{\dot{Q}_{loss}}{T_\infty} + \dot{m}c_{p0}\ln\left(T_6/T_5\right) - \dot{m}R\ln\left(P_6/P_5\right)\right]_{receiver} \\ &+ \left[-\dot{m}c_{p0}\ln\left(T_7/T_8\right) + \dot{m}R\ln\left(P_7/P_8\right)\right]_{turbine}\end{aligned} \tag{17}$$

The overall efficiency is determined with Equation (18) where $\eta_{th} = \dot{W}_{net}/\dot{Q}_{net}$ and $\eta_{solar} = \dot{W}_{net}/\dot{Q}^*$. The receiver efficiency is determined with Equation (19).

$$\eta_{STBC} = \eta_{refl}\eta_{optical}\eta_{rec}\eta_{th} = \eta_{refl}\eta_{optical}\eta_{solar}, \tag{18}$$

$$\eta_{rec} = \dot{Q}_{net}/\dot{Q}^* = \dot{m}c_{p0}\left(T_6 - T_5\right)/\eta_{optical}\eta_{refl}\dot{Q}_{solar}. \tag{19}$$

3. Results

Figures 6-8 show the maximum thermal efficiency of the cycle for different micro-turbines operating at different turbine pressure ratios and receiver tube surface temperatures. Note that the

maximum thermal efficiency is presented for each turbine pressure ratio, which is represented by an optimum recuperator geometry. Table 4 also shows the maximum thermal efficiency at different turbine pressure ratios for the *GT2052* and T_s = 900 K (compare with Fig. 7).

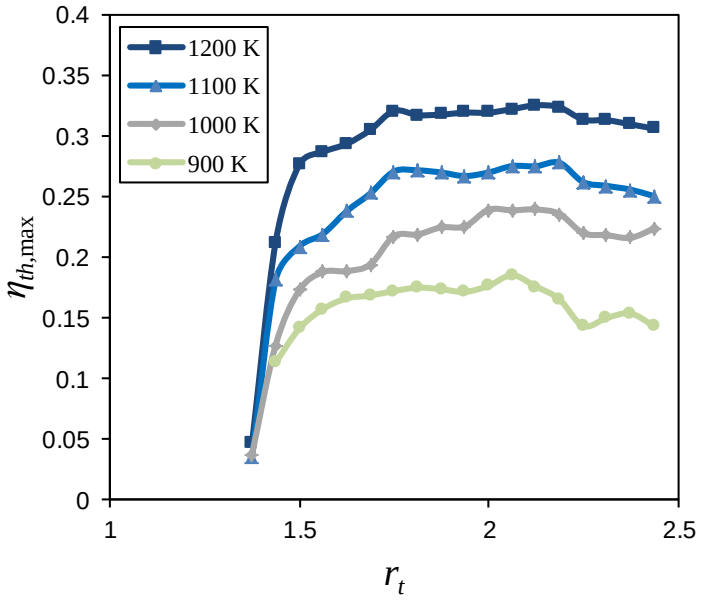

Fig. 6 Maximum thermal efficiency of the cycle for different turbine pressure ratios and for receiver tube surface temperatures from 900 K to 1200 K (for *GT1241*).

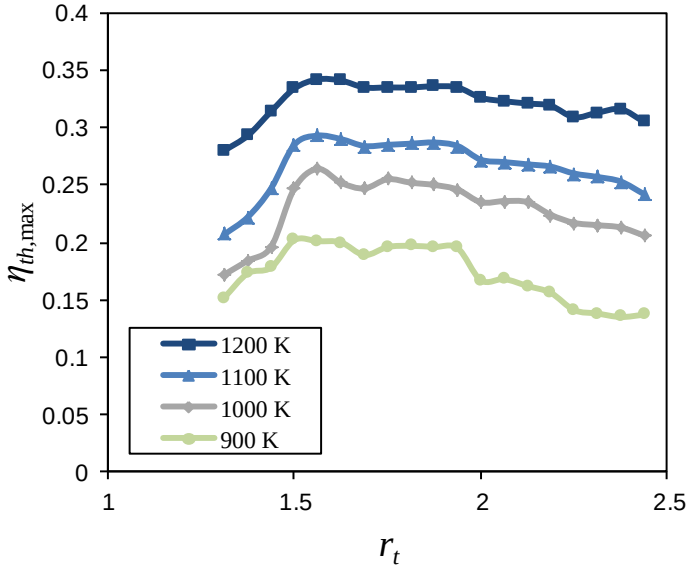

Fig. 7 Maximum thermal efficiency of the cycle for different turbine pressure ratios and for receiver tube surface temperatures from 900 K to 1200 K (for *GT2052*).

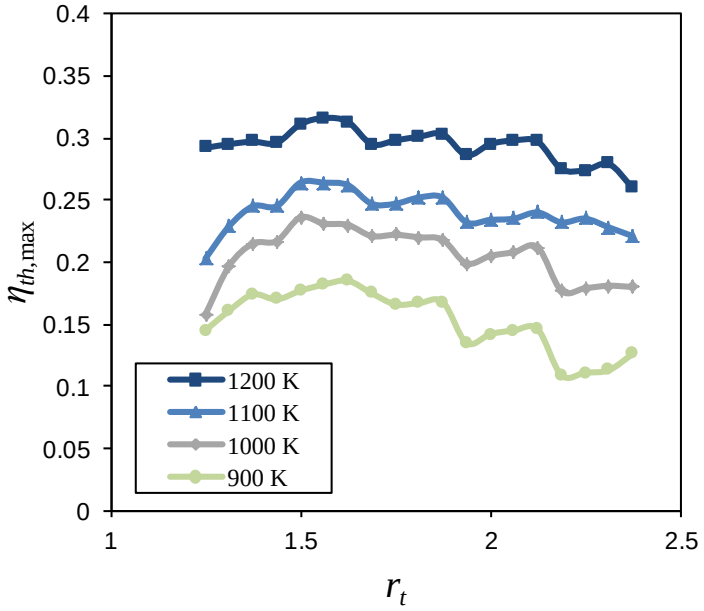

Fig. 8 Maximum thermal efficiency of the cycle for different turbine pressure ratios and for receiver tube surface temperatures from 900 K to 1200 K (for *GT2860RS*).

Table 4 Optimum recuperator geometries for maximum thermal efficiency at different turbine operating points, for *GT2052* and T_s = 900 K.

r_t	a (mm)	b (mm)	L_{reg} (m)	n	$\dot{W}_{net}$ (W)	Mass (kg)	$\dot{Q}_{net}$ (kW)	$\eta_{th,\max}$
1.5	225	2.25	1.5	45	1081	491	5.4	0.202
1.94	225	2.25	1.5	45	2201	491	11.3	0.195
2.38	225	2.25	1.5	45	2377	491	17.6	0.135

For a range of turbine pressure ratios, different recuperator geometries were considered so that the optimum geometry, which would produce the maximum thermal efficiency, could be found. Table 5 shows, for example, the results for a recuperator where the channel width (a) is 225 mm, the channel height (b) is 2.25 mm, the length (L_{reg}) is 1.5 m and the number of parallel flow channels (n) is 45. For these recuperator dimensions, the cycle produces a maximum thermal efficiency of 20.2% at the pressure ratio of 1.5 for the *GT2052*, when the receiver tube surface temperature is 900 K. This maximum also appears in Table 4.

Table 5 Net power output and net heat transfer rate for different recuperator geometries where r_t = 1.5, *GT2052* and T_s = 900 K.

r_t	a (mm)	b (mm)	L_{reg} (m)	n	$\dot{W}_{net}$ (W)	Mass (kg)	$\dot{Q}_{net}$ (kW)	η_{th}
1.5	150	3.75	4.5	15	1033	332	7.2	0.143
1.5	225	2.25	1.5	45	1081	491	5.4	0.202
1.5	300	3.00	1.5	22.5	1119	327	6.4	0.176
1.5	375	3.75	1.5	22.5	1142	409	6.5	0.177
1.5	450	1.5	1.5	15	902	325	5.7	0.158

Table 6 Net power output and net heat transfer rate for different recuperator geometries where r_t = 1.5, *GT2052* and T_s = 900 K (lighter alternatives).

r_t	a (mm)	b (mm)	L_{reg} (m)	n	$\dot{W}_{net}$ (W)	Mass (kg)	$\dot{Q}_{net}$ (kW)	η_{th}
1.5	150	1.5	3	15	1116	110	9.3	0.120
1.5	150	2.25	1.5	15	1016	164	7.2	0.141
1.5	300	2.25	1.5	15	1045	218	6.6	0.158
1.5	150	2.25	1.5	30	1034	219	6.4	0.161
1.5	150	2.25	1.5	37.5	1049	274	6.0	0.174
1.5	225	2.25	1.5	30	1063	327	5.8	0.183

Table 7 Maximum thermal efficiency for *GT1241* and different surface temperatures.

T_s (K)	$r_{t,opt}$	a (mm)	b (mm)	L_{reg} (m)	n	$\dot{W}_{net}$ (W)	Mass (kg)	$\dot{Q}_{net}$ (kW)	$\dot{Q}^*$ (kW)	$\eta_{th,max}$
900	2.063	225	2.25	1.5	45	1351	491	7.3	12.3	0.185
1000	2.125	225	2.25	1.5	45	1986	491	8.3	15.3	0.239
1100	2.188	225	2.25	1.5	45	2556	489	9.2	18.2	0.277
1200	2.125	225	1.50	1.5	45	2928	489	9	21	0.325

Table 8 Maximum thermal efficiency for *GT2052* and different surface temperatures.

T_s (K)	$r_{t,opt}$	a (mm)	b (mm)	L_{reg} (m)	n	$\dot{W}_{net}$ (W)	Mass (kg)	$\dot{Q}_{net}$ (kW)	$\dot{Q}^*$ (kW)	$\eta_{th,max}$
900	1.5	225	2.25	1.5	45	1081	491	5.4	10.4	0.202
1000	1.563	225	2.25	1.5	45	1772	491	6.7	13.7	0.264
1100	1.563	225	2.25	1.5	45	2050	491	7.0	16.0	0.293
1200	1.563	225	1.50	1.5	45	2449	489	7.2	19.2	0.342

Table 9 Maximum thermal efficiency for *GT2860RS* and different surface temperatures.

T_s (K)	$r_{t,opt}$	a (mm)	b (mm)	L_{reg} (m)	n	$\dot{W}_{net}$ (W)	Mass (kg)	$\dot{Q}_{net}$ (kW)	$\dot{Q}^*$ (kW)	$\eta_{th,\max,\max}$
900	1.625	225	2.25	1.5	45	2051	491	11.1	16.1	0.185
1000	1.500	225	2.25	1.5	45	2131	491	9	16.0	0.236
1100	1.500	225	2.25	1.5	45	2484	491	9.4	18.4	0.264
1200	1.563	225	2.25	1.5	45	3665	491	11.6	23.6	0.316

Table 6 shows that there are a number of alternative recuperators which are much lighter and can still produce an acceptable thermal efficiency (compare with Table 5). A recuperator of 274 kg produces a thermal efficiency of 17.4%, while the optimum recuperator with a mass of 491 kg produces 20.2%. Furthermore, Tables 7-9 show the maximum thermal efficiencies and optimum turbine pressure ratios that were found for each micro-turbine at different receiver tube surface temperatures (compare with Figs. 6-8). The results show that a recuperator with channel width of 225 mm, channel height of 2.25 mm, length of 1.5 m and with 45 parallel flow channels usually performs well to produce a maximum thermal efficiency, which shows that a shorter recuperator with more flow channels performs best. This result was also found by Le Roux et al. (2014b) for a recuperated solar-dish Brayton cycle without phase-change material in the receiver using a 4.8-m dish diameter. Tables 7-9 also show that the *GT2052* outperforms the other two turbochargers in terms of maximum thermal efficiency.

Figure 9 shows the heat losses from the receiver with a fixed aperture area of 0.25 m × 0.25 m. Radiation heat loss dominates at receiver temperatures of 950 K and upwards and therefore the total heat loss increases drastically at higher temperatures. From Figs. 6-8 however, it was shown that the thermal efficiency of the cycle increases as the tube surface temperature increases. For each different micro-turbine, Figs. 10-12 therefore show the cycle's net power output at maximum thermal efficiency, as a function of turbine pressure ratio, together with the solar power required at the receiver aperture, $\dot{Q}^*$. The results indicate that more power can be produced at higher pressure ratios and higher receiver surface temperatures, however, at higher receiver surface temperatures, the required solar input, $\dot{Q}^*$, increases due to increased heat losses. Furthermore, $\dot{Q}^*$ represents the cost of the solar dish and its solar tracking system

because the aperture area of the receiver is fixed at 0.25 m × 0.25 m. An increased $\dot{Q}^*$ therefore represents a larger solar dish with higher required accuracy. Figures 10-12 are therefore performance maps for each micro-turbine relative to the initial cost of the solar collector.

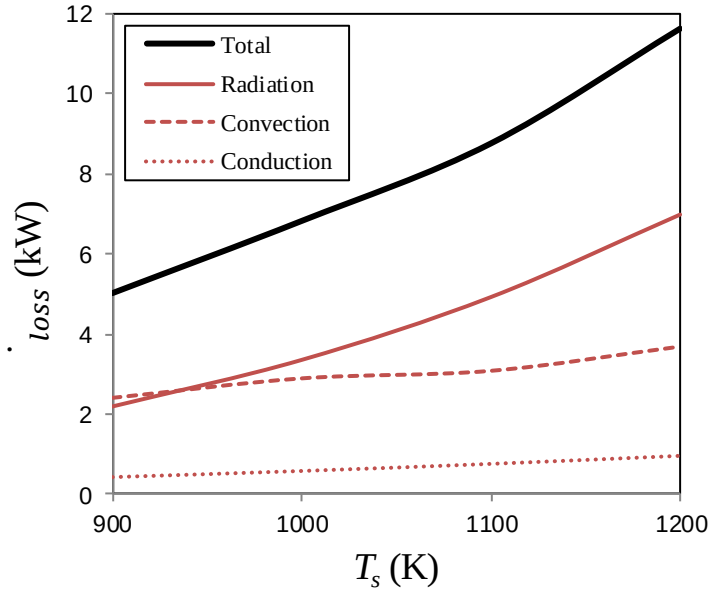

Fig. 9 Heat loss rate from the solar receiver as a function of tube surface temperature.

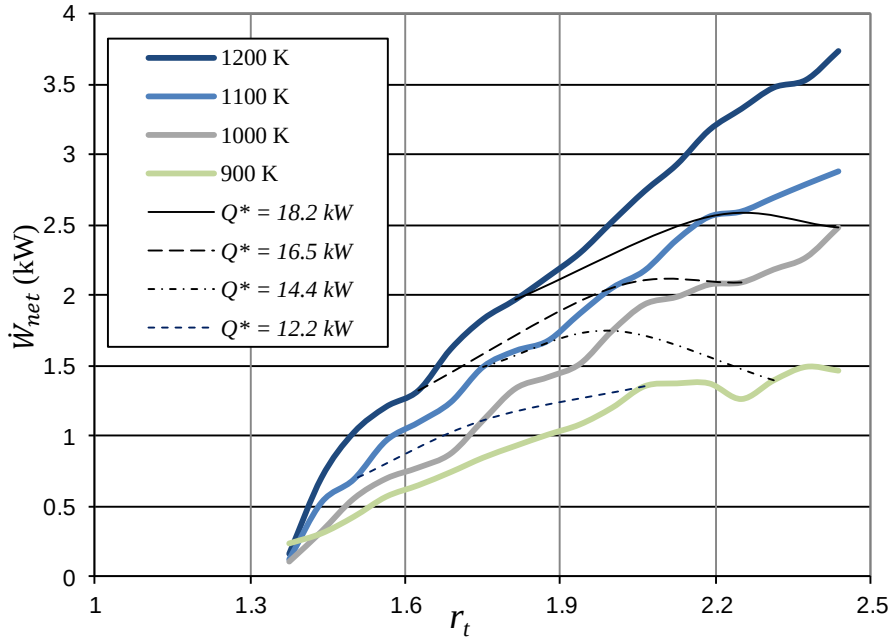

Fig. 10 Net power output at maximum thermal efficiency as a function of turbine pressure ratio, receiver tube surface temperatures (900-1200 K) and solar input power, $\dot{Q}^*$ (for *GT1241*).

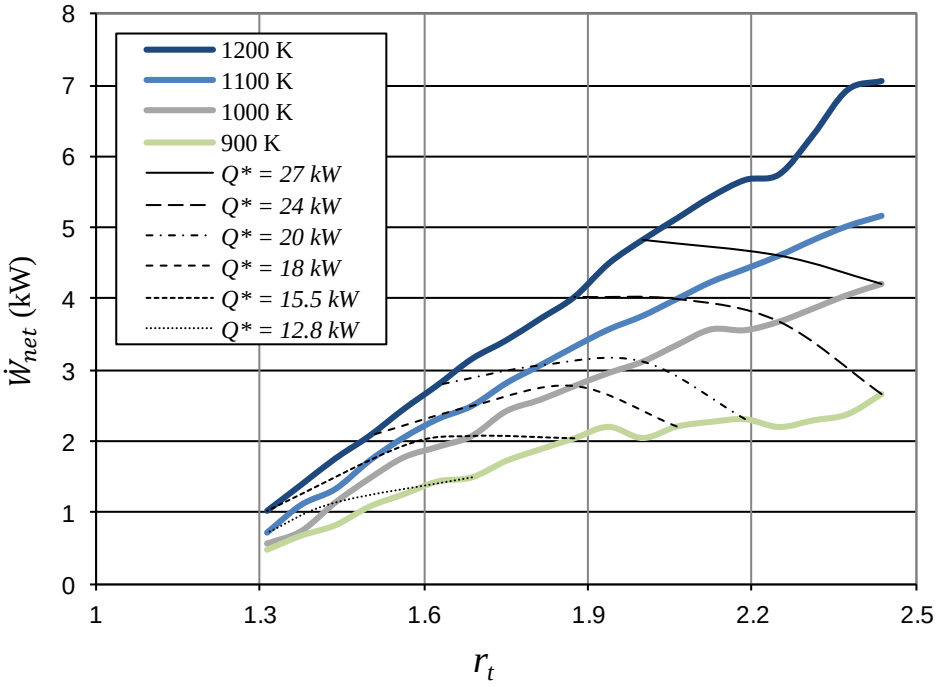

Fig. 11 Net power output at maximum thermal efficiency as a function of turbine pressure ratio, receiver tube surface temperatures (900-1200 K) and solar input power, $\dot{Q}^*$ (for *GT2052*).

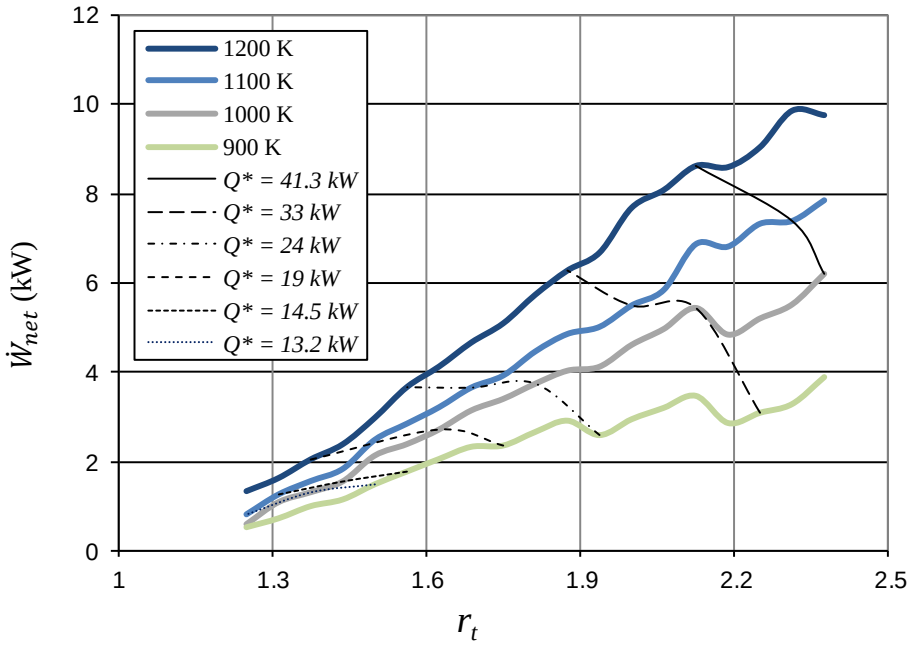

Fig. 12 Net power output at maximum thermal efficiency as a function of turbine pressure ratio, receiver tube surface temperatures (900-1200 K) and solar input power, $\dot{Q}^*$ (for *GT2860RS*).

The maps allow for the selection of the thermal storage temperature for an expected solar input power. For example, in Fig. 11, where the required solar input power is $\dot{Q}^*$ = 12.8 kW (a small low-cost solar dish), 1.5 kW shaft power can be produced at a low temperature of 900 K, while only 1.15 kW shaft power can be produced at 1000 K. The solar conversion efficiency at 900 K would be 12% (assuming perfect solar dish reflection). Figure 11 also shows that a maximum of 7.1 kW of power can be produced when the receiver surface temperature is chosen as 1200 K; however, the required solar input power would be 35.1 kW. This would require a much larger, more accurate and expensive solar dish (aiming at the same 0.25 m × 0.25 m aperture) and the solar conversion efficiency would be 20.1%. It is clear that these maps can be used in a cost analysis.

Figures 13-15 show the maximum solar conversion efficiency for each turbocharger. Note that the solar dish reflectivity as well as optical efficiency (intercept factor) is not included in this efficiency. The maximum solar conversion efficiencies increase as the receiver surface temperature increases, especially at higher turbine pressure ratios and higher receiver surface temperatures. Figure 14 shows that solar conversion efficiencies of up to 13.5% can be achieved (at 900 K) with the *GT2052* operating at a turbine pressure ratio of 1.94. The thermal efficiency at this pressure ratio is η_{th} = 19.5% according to Table 4, with 2.2 kW of shaft power. For this setup operating at lower temperature, less expensive materials would be required and the solar dish would not have to be very expensive (or accurate) either. Figure 15 shows that solar conversion efficiencies of up to 21% can be achieved (at 1200 K) with an off-the-shelf turbocharger (the *GT2860RS*) operating at a turbine pressure ratio of 2.125; however, the required solar power is 41 kW, which means the solar dish and tracking system would have to be very accurate and expensive. Note that the efficiency could be further improved by doing specific compressor and turbine pairing, since the current work only considers the off-the-shelf compressor and turbine pair.

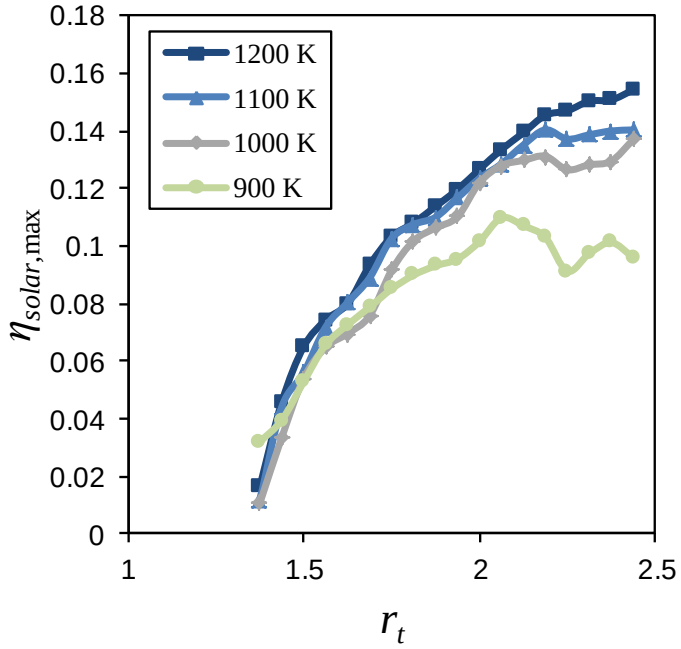

Fig. 13 Maximum solar conversion efficiency efficiency for different turbine pressure ratios and receiver tube surface temperatures of 900 K to 1200 K (for *GT1241*).

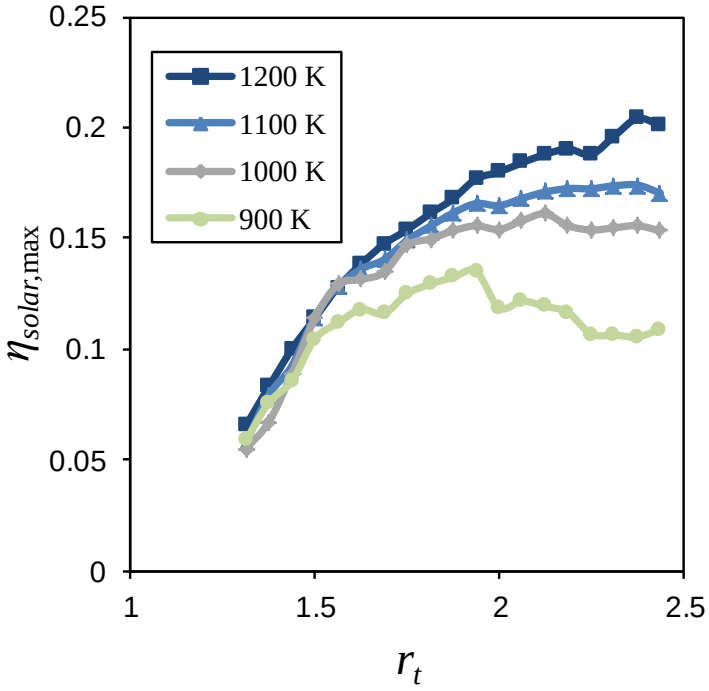

Fig. 14 Maximum solar conversion efficiency efficiency for different turbine pressure ratios and receiver tube surface temperatures of 900 K to 1200 K (for *GT2052*).

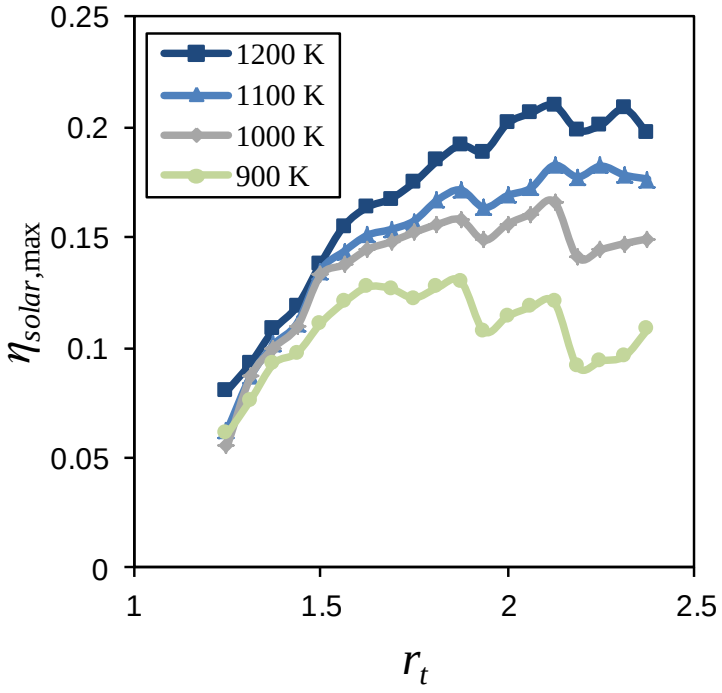

Fig. 15 Maximum solar conversion efficiency efficiency for different turbine pressure ratios and receiver tube surface temperatures of 900 K to 1200 K (for *GT2860RS*).

Figure 16 shows the temperatures at the different positions in the cycle (with reference to Fig. 1) for performance at maximum thermal efficiency when using a *GT2052* as micro-turbine with the recuperators listed in Table 8. The figure shows that the recuperator is responsible for most of the temperature rise before the compressed air flows into the turbine. Furthermore, the air leaving the cycle is still at around 373 K, which leaves much potential for cogeneration in terms of water heating. The figure also shows that there is a difference between the receiver air exit temperature and the receiver surface temperature, because of the low heat transfer coefficient in the solar receiver. However, according to Fig. 17, the large receiver tube allows for minimum pressure drop in the receiver, which allows for maximum inlet pressure at the turbine. Figure 17 also shows that the colder receiver operates at a lower pressure and that the pressure drop through both the recuperator and solar receiver is small.

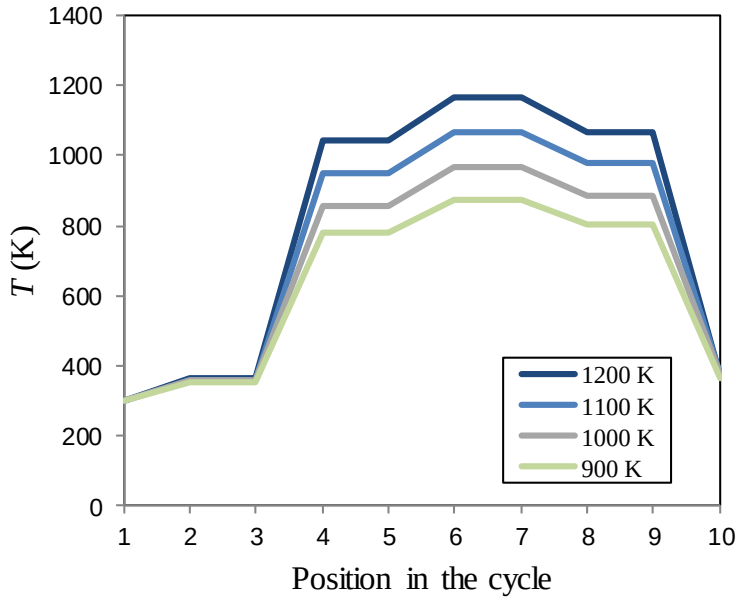

Fig. 16 Temperature in the cycle at different receiver surface temperatures for maximum thermal efficiency (for *GT2052*).

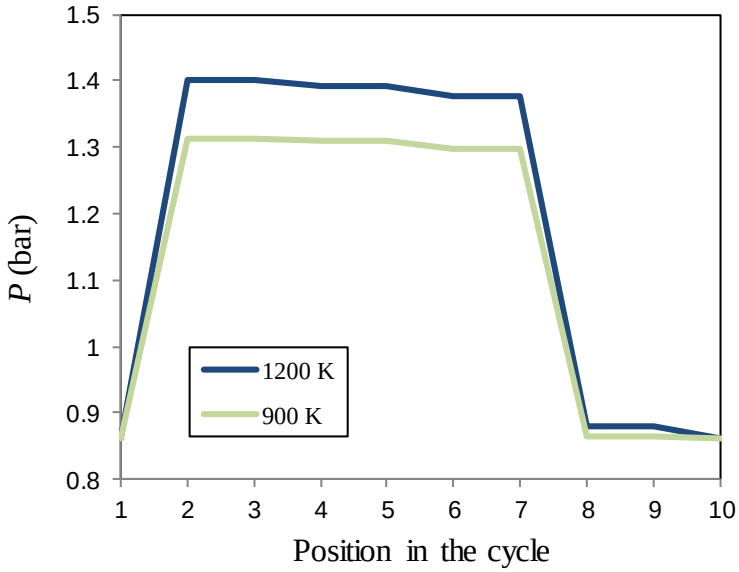

Fig. 17 Pressure in the cycle at different receiver surface temperatures for maximum thermal efficiency (for *GT2052*).

Table 10 shows a few of the important parameters for the cycle running at maximum thermal efficiency using the *GT2052* and the optimum recuperator dimensions as shown in Table 8. The

heat transfer coefficients in the recuperator are lower at lower receiver temperatures and the optimum speed at all receiver temperatures is 120 000 rpm.

Table 10 Performance at maximum efficiency for *GT2052* at different surface temperatures.

	900 K	**1000 K**	**1100 K**	**1200 K**
N (rpm)	120 000	120 000	120 000	120 000
$\dot{m}$ (kg/s)	0.0512	0.0529	0.0504	0.0491
η_t	0.700	0.691	0.682	0.670
η_c	0.700	0.702	0.697	0.690
r_c	1.526	1.593	1.594	1.631
r_t	1.5	1.5625	1.5625	1.5625
h_{rec} (W/m^{2}K)	40.3	42.4	41.8	41.7
$h_{reg,h}$ (W/m^{2}K)	83.3	88.3	93.4	146.3
$h_{reg,c}$ (W/m^{2}K)	81.1	85.7	90.7	143.3

Overall, the results show that an open-cavity tubular solar receiver with metallic phase-change thermal storage material can be used together with an off-the-shelf turbocharger for power generation in a recuperated solar-dish Brayton cycle. Results show that higher receiver surface temperatures do have an advantage in terms of the overall solar conversion efficiency, but that a larger and more accurate solar dish would be required for steady-state operation (since the receiver aperture geometry is fixed). Lower receiver operating temperatures therefore have an advantage in terms of cost, especially when considering that for a recuperator hot-side inlet temperature of less than 950 K, stainless steel materials can be used instead of super-alloys (Shah, 2005).

4. Case study

Table 11 shows potential metals and alloys to be used as thermal storage for a solar-dish Brayton cycle. Each thermal storage material, listed in Table 11, will introduce its own challenges in terms of weight and cost, containment material selection (Andraka et al., 2015), as well as charging and discharging times depending on the local solar resource.

Table 11 Potential phase-change materials: metals and metal alloys (Khare et al. 2012; Farkas and Birchenall, 1985, cited in Cárdenas and León, 2013; Gasanealiev and Gamataeva, 2000, cited in Liu et al., 2012 and Cárdenas and León, 2013).

Phase-change material	Composition (wt%)	Melting temperature (K)	ρ (kg/m^3)	$c_{p,solid}$ (J/kgK)	$c_{p,liquid}$ (J/kgK)	k (W/mK)	Latent heat, L_f (kJ/kg)
Mg		921	1740	1270	1370		365
Al		933	2700	900	1100	186	397
Zn–Cu–Mg	49/45/6	976	8670	420			176
Cu–P	91/9	988	5600				134
Cu–Zn–P	69/17/14	993	7000				368
Cu–Zn–Si	74/19/7	1038	7170				125
Cu–Si–Mg	56/27/17	1043	4150	750			420
Mg–Ca	84/16	1063	1380				272
Mg–Si–Zn	47/38/15	1073					314
Cu–Si	80/20	1076	6600	500			197
Cu–P–Si	83/10/7	1113	6880				92
Si–Mg–Ca	49/30/21	1138	2250				305
Si-Mg	56/44	1219	1900	790		70	757

Figure 18 shows the theoretical storage time, t_{PC}, available at the phase-change temperature as a function of the rate at which the phase-change material would receive or loose heat, $\dot{Q}$, according to Equation (20). The figure therefore shows how long it will take for each phase-change material to fully charge (melt) and fully discharge (solidify) at the constant phase-change temperature. Four materials that are light-weight and have an acceptable storage time are shown. Note that a phase-change-material volume of V_{PCM} = 0.05 m^3 is assumed, which can be placed around the receiver tube (according to Fig. 3).

$$t_{PC} = \rho V_{PCM} L_f \left/ \dot{Q} \right. \tag{20}$$

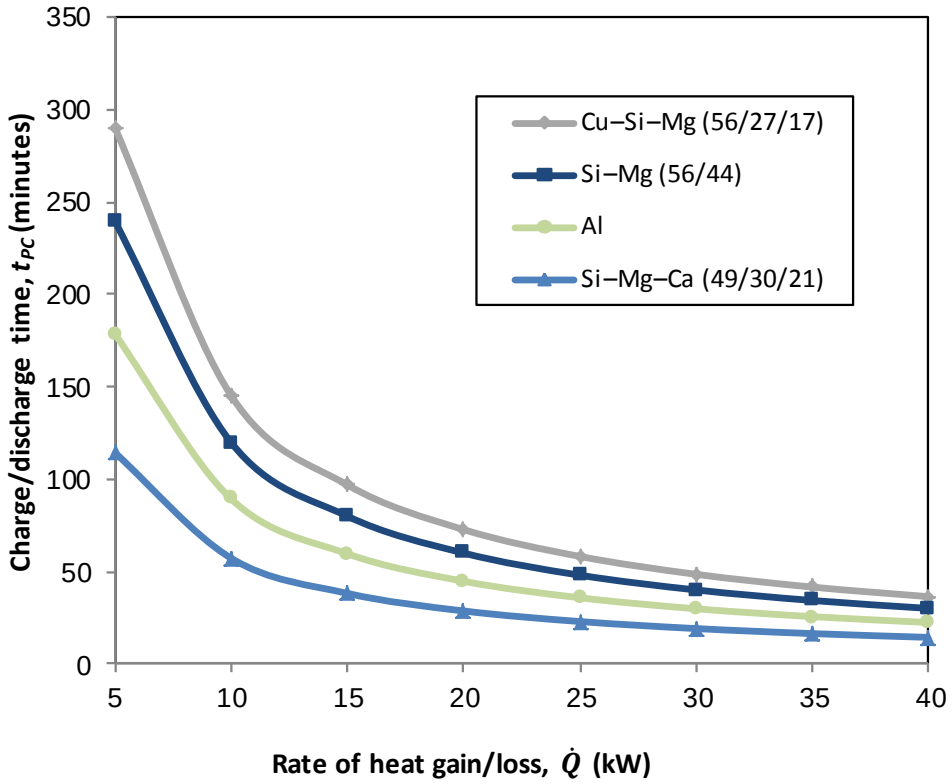

Fig. 18 Thermal storage time available at the phase-change temperature for light-weight phase-change materials.

As an example (Case 1), a recuperated solar-dish Brayton cycle using a *GT2052* turbocharger with aluminium in the receiver is considered (see Table 12). The storage material mass is 135 kg. Suppose a low-cost, low efficiency system is sought then, according to Fig. 11 at 933 K, a steady-state solar input power of $\dot{Q}^* \approx 14$ kW can be used to generate a power output of $\dot{W}_{net} \approx$ 1.75 kW. If a solar dish reflectivity of 90% and intercept factor of 90% is assumed, $\dot{Q}_{solar} \approx 17.5$ kW and therefore a 17.5 m^2 solar dish is required (assuming a design irradiance of 1000 W/m^2). The overall solar conversion efficiency would be 10%. The proposed system can be supplemented with gas as a hybrid when solar irradiance levels are low. The proposed system can have minimum cost since the concentration ratio (≈280) would not require a very accurate solar dish. Low dish accuracy will decrease the costs of the solar dish significantly. The use of a coiled tube receiver and turbocharger as micro-turbine already allows for a significant cost reduction. Operation at lower temperature further reduces the costs in terms of material

requirements. According to Fig. 18, the receiver would be able to operate at 933 K for about 65 minutes after cloudy weather arrives (then $\dot{Q}^* \approx 14$ kW is supplied from the thermal storage instead of the sun), if it was fully charged. According to Fig. 9 and Fig. 18, the receiver should be able to operate for about 100 minutes after cloudy weather arrives, if it was fully charged and the receiver aperture closed off to prevent radiation and convection heat losses (then $\dot{Q}^* = \dot{Q}_{net} + \dot{Q}_{loss,cond} \approx 9$ kW).

Table 12 Case study showing three scenarios and the application of the performance maps.

	Case 1	**Case 2**	**Case 3**
Turbocharger	*GT2052*	*GT2050*	*GT2860RS*
Phase-change material	Al (933 K)	Cu-Si-Mg (1043 K)	Si-Mg (1219 K)
$\dot{W}_{net}$ (kW)	1.75	3.3	8.8
r_t	≈1.7	≈2	≈2.1
$\dot{Q}_{net}$ (kW)	8.5	12.3	29.3
$\dot{Q}_{loss}$ (kW)	5.5	7.7	12.0
Required $\dot{Q}^*$ (kW)	14 kW	20 kW	41 kW
Required $\dot{Q}_{solar}$ (kW)	17.5 kW	24.7 kW	50.6 kW
Required dish size	17.5 m^2	24.7 m^2	50.6 m^2
Overall solar conversion efficiency	10%	13%	17%
Concentration ratio	280	395	778
Storage time with aperture open	65 minutes	73 minutes	30 minutes
Storage time with aperture closed	≈100 minutes (at $\dot{Q}^* \approx 9$ kW)	≈112 minutes (at $\dot{Q}^* \approx 13$ kW)	≈50 minutes (at $\dot{Q}^* \approx 30$ kW)
Storage material mass	135 kg	208 kg	95 kg

As another example, a recuperated solar-dish Brayton cycle using a *GT2860RS* with Si-Mg in the receiver is considered (see Table 12) where a very efficient, high-cost system is sought.

According to Fig. 9, Fig. 12 and Fig. 18, the overall solar conversion efficiency would be 17% with 30-40 minutes of storage time and a storage mass of 95 kg. This result compares well with Bashir et al. (2019) who found a 30 minute storage time for Si-Mg, based on a 41 L storage volume and a $\dot{Q}*$ of 30 kW. As another example, a recuperated solar-dish Brayton cycle using a *GT2052* with Cu-Si-Mg in the receiver is considered for a system with an average efficiency and average cost relative to the previous two examples. An overall solar conversion efficiency of 13% is found with 73-112 minutes of storage time and a mass of 208 kg. However, it should be noted that some reports of the solidification behavior in Cu-Si-Mg alloys suggest that it may solidify initially as a two-phase eutectic (Gibbs et al., 2016). It is clear that each thermal storage material, listed in Table 11, will introduce its own challenges.

Note that the efficiencies mentioned above could be further improved by doing specific compressor and turbine pairing, since the current work only considered the off-the-shelf compressor and turbine pair. Even so, the solar-to-mechanical conversion efficiencies are low relative to competing technologies such as dish-Stirling with a record of 31.25% (Andraka et al., 2015). However, the solar-dish Brayton cycle with turbocharger can operate during the night using combustion of gas as a hybrid system, has significant potential for cogeneration and has an advantage in terms of cost and low maintenance (Mills, 2004; Visser et al., 2011). Furthermore, the addition of thermal storage allows for stable operation when the solar irradiance is fluctuating and allows for continued operation when the sun has set (when there is a peak in electricity demand). The development by Visser et al. (2011), where a turbocharger was used for a micro gas recuperated CHP application, has led to a commercial 3.2 kWe recuperated Brayton cycle with 15.6 kW water heating capacity, which requires 20 kW heat input (a total efficiency or energy utilization factor of 94%). It is clear that further optimization can be done to determine which configuration will allow for the most cost-effective solar-dish Brayton cycle with cogeneration, which could allow for high overall solar-to-CHP efficiencies. The *GT2052* operating with molten aluminum in the receiver at 933 K, could be worth investigating further as a simple and low-cost solar-gas hybrid Brayton cycle configuration with cogeneration; however, a suitable containment material with proper surface coating should be used as was suggested by Yan and Fan (2001) and Fu et al., (2017).

5. Conclusion

The recuperated solar-dish Brayton cycle has a cost advantage because of high production quantities of turbochargers in the vehicle industry. Three different off-the-shelf turbochargers and different recuperator geometries were considered in this paper to determine the maximum thermal efficiency of a recuperated solar-dish Brayton cycle with a fixed solar receiver geometry operating at different phase-change temperatures. Metallic phase-change material of high conductivity was proposed as thermal storage material which can be placed around a low-cost coiled tube in an open-cavity solar receiver. A performance map was developed for each turbocharger which allows for the assessment of the cycle in terms of cost, power output, pressure ratio and phase-change temperature. Results showed that maximum thermal efficiencies of 20.2% to 34.2% and solar conversion efficiencies of 13.5% to 21% (11% to 17% when dish reflectivity and intercept factor are both assumed 90%) can be achieved at receiver temperatures of between 900 K and 1200 K. It is suggested that further optimization and experimental investigation be done on a solar-gas hybrid Brayton cycle with cogeneration, using the *GT2052* and operating with molten aluminium in the receiver as a low-cost and low-complexity solution.

References

Allen, K.G., 2010. Performance characteristics of packed bed thermal energy storage for solar thermal power plants. Thesis: University of Stellenbosch.

Andraka, C.E., Rawlingson, K.S. and Siegel, N.P., 2012. Technical feasibility of storage on large dish Stirling systems. Sandia National Laboratories, Report: SAND2012-8352, Albuquerque, New Mexico.

Andraka, C.E., 2014. Dish Stirling advanced latent storage feasibility, *Energy Procedia* 49, pp. 684-693.

Andraka, C.E., Kruizenga, A.M., Hernandez-Sanchez, B.A. and Coker, E.N., 2015. Metallic Phase Change Material Thermal Storage for Dish Stirling. *Energy Procedia* 69, pp. 726-736.

Asselman, G.A.A., 1976. Thermal energy storage unit based on lithium fluoride. *Energy Conversion* 16, pp. 35-47.

Bashir, M.A., Giovannelli, A. and Ali, H.M., 2019. Design of high-temperature solar receiver integrated with short-term thermal storage for dish-micro gas turbine systems. *Solar Energy* 190, pp. 156-166.

Batteh, J.J. and Newman, C.E., 2008. Detailed simulation of turbocharged engines with Modelica, (March 3 and 4), The Modelica Association.

Bejan, A., 2006. Advanced Engineering Thermodynamics, 3rd ed., New York: John Wiley & Sons, Inc.

Cameron, H.M., Mueller, L.A., Namkoong, D., 1972. Preliminary design of a solar heat receiver for a Brayton-cycle space power system. Report NASA TM X-2552, National Aeronautics and Space Administration, Lewis Research Center.

Cárdenas, B. and León, N., 2013. High temperature latent heat thermal energy storage: Phase change materials, design considerations and performance enhancement techniques. *Renewable and Sustainable Energy Reviews* 27, pp. 724-737.

Carpenter, A.L., Beechner, T.L., Tews, B.E. and Yelvington, P.E., 2018. Hybrid-electric turbocharger and high-speed SiC variable frequency drive using sensorless control algorithm. *Journal of Engineering for Gas Turbines and Power* 140, pp. 122801:1-8.

Çengel, Y.A., 2006. Heat and mass transfer. 3rd ed. Nevada: McGraw-Hill.

Chen, L., Zhang, W., Sun, F., 2007. Power, efficiency, entropy-generation rate and ecological optimization for a class of generalized irreversible universal heat-engine cycles, *Applied Energy* 84, pp. 512-525.

Coventry, J. and Andraka, C., 2017. Dish systems for CSP. *Solar Energy* 152, pp. 140-170

Dickey, B., 2011. Test results from a concentrated solar microturbine Brayton cycle integration, Proceedings of the ASME Turbo Expo, Vol. 3, pp. 1031-1036.

Farkas, D., Birchenall, C.E., 1985. New eutectic alloys and their heats of transformation. *Metallurgical and Material Transactions A* 16, pp. 323-328.

Fluri, T.P., 2009. The potential of concentrating solar power in South Africa. *Energy Policy* 37, pp. 5075-5080.

Fu, G., Wu, Y., Liu, Q., Li, R. and Su, Y. 2017. Hot corrosion behavior of stainless steel with Al-Si/Al-Si-Cr coating, *High Temp. Mater. Proc.* 36(3), pp. 243-248.

Garrett, 2014. Garrett by Honeywell: Turbochargers, Intercoolers, Upgrades, Wastegates, Blow-Off Valves, Turbo-Tutorials. Available at: http://www.TurboByGarrett.com. [Last accessed on 2014/08/22].

Gasanealiev, A.M., Gamataeva, B.Y., 2000. Heat-accumulating properties of melts. *Russian Chemical Reviews* 69, pp. 179-86.

Gavagnin, G., Rech, S., Sánchez, D. and Lazzaretto, A., 2018. Optimum design and performance of a solar dish microturbine using tailored component characteristics. *Applied Energy* 231, pp. 660-676.

Gibbs, P.J., Withey, E.A., Coker, E.N., Kruizenga, A.M. and Andraka, C.E., 2016. Copper-silicon-magnesium alloys for latent heat storage, *Metallurgical and Materials Transactions* 3E, pp. 273-280.

Giovannelli, A., Bashir, M.A., Archilei, E.M., 2017. High-temperature solar receiver integrated with a short-term storage system, AIP Conference Proceedings 1850, 050001; doi: 10.1063/1.4984405.

Guzzella, L. and Onder, C.H., 2010. Introduction to modeling and control of internal combustion engine systems, 2nd ed. Berlin, Germany: Springer-Verlag;

Harris, J.A., Lenz, T.G., 1983. Thermal performance of solar concentrator/cavity receiver systems, *Solar Energy* 34 (2), pp. 135-142.

Heller, P., Pfänder, M., Denk, T., Tellez, F., Valverde, A., Fernandez, J. et al., 2006. Test and evaluation of a solar powered gas turbine system. *Solar Energy* 80, pp. 1225-1230.

Jilte, R.D., Kedare, S.B., Nayak, J.K., 2013. Natural convection and radiation heat loss from open cavities of different shapes and sizes used with dish concentrator. *Mechanical Engineering Research* 3(1), pp. 25-43.

Khare, S., Dell'Amico, M., Knight, C. and McGarry, S., 2012. Selection of materials for high temperature latent heat energy storage. *Solar Energy Materials & Solar Cells* 107, pp. 20-27.

Klein, P., 2016. High temperature packed bed thermal storage for solar gas turbines. Thesis: University of the Witwatersrand.

Korzynietz, R. et al., 2016. Solugas – Comprehensive analysis of the solar hybrid Brayton plant, *Solar Energy* 135, pp. 578-589.

Lanchi et al., 2015. Investigation into the coupling of Micro Gas Turbines with CSP technology: OMSoP project, *Energy Procedia* 69, pp. 1317-1326.

Le Roux, W.G., Bello-Ochende, T. and Meyer, J.P., 2014a. The efficiency of an open cavity solar receiver for a small-scale solar thermal Brayton cycle, *Energy Conversion and Management* 84, 457-470.

Le Roux, W.G., Bello-Ochende, T. and Meyer, J.P., 2014b. Optimisation of an open rectangular cavity receiver and recuperator used in a small-scale solar thermal Brayton cycle with thermal losses, 10th International Conference on Heat Transfer, Fluid Mechanics and Thermodynamics (HEFAT2014), Orlando, Florida, 14-16 July.

Le Roux, W.G., 2015. Thermodynamic optimisation and experimental collector of a dish-mounted small-scale solar thermal Brayton cycle, Thesis: University of Pretoria.

Le Roux, W.G. and Meyer, J.P., 2016. Modeling the Small-Scale Dish-Mounted Solar Thermal Brayton Cycle, AIP Conference Proceedings 1734, 060002; doi: 10.1063/1.4949144.

Le Roux, W.G., 2018. Feasibility study of a hybrid small-scale dish-mounted solar thermal Brayton cycle with cogeneration, Proceedings of the 16th International Heat Transfer Conference (IHTC16-24185), Beijing, China, pp. 7929-7936.

Lidsky, L.M., Lanning, D.D., Staudt, J.E., Yan, X.L., Kaburaki, H., Mori, M., et al., 1991. A direct-cycle gas turbine power plant for near-term application: MGR-GT, *Energy* 16, pp.177-86.

Liu, M., Saman, W. and Bruno, F., 2012. Review on storage materials and thermal performance enhancement techniques for high temperature phase change thermal storage systems. *Renewable and Sustainable Energy Reviews* 16, pp. 2118-2132.

Loni, R., Asli-Ardeh, E.A., Ghobadian, B., Ahmadi, M.H. and Bellos, E., 2018. GMDH modeling and experimental investigation of thermal performance enhancement of hemispherical cavity receiver using MWCNT/oil nanofluid, *Solar Energy* 171, pp. 790-803.

Malali, P.D., Chaturvedi, S.K. and Abdel-Salam, T., 2017. Performance optimization of a regenerative Brayton heat engine coupled with a parabolic dish solar collector, *Energy Conversion and Management* 143, pp. 85-95.

McDonald, C.F. and Rodgers, C., 2002. The ubiquitous personal turbine - a power vision for the 21st century, *Journal of Engineering for Gas Turbines and Power* 124, pp. 835-844.

McDonald, C.G., 1995. Heat loss from an open cavity, SAND95-2939, Sandia National Laboratories, Report: SAND95-2939, Albuquerque, New Mexico.

Mills, D., 2004. Advances in solar thermal electricity technology, *Solar Energy* 76, pp. 9-31.

Nellis, G.F. and Pfotenhauer, J.M., 2005. Effectiveness-NTU relationship for a counterflow heat exchanger subjected to an external heat transfer, *Journal of Heat Transfer* 127, pp. 1071-1073.

Nelson, J., Johnson, N.G., Doron, P. and Stechel, E.B., 2018. Thermodynamic modeling of solarized microturbine for combined heat and power applications, *Applied Energy* 212, pp. 592-606.

Ozturk, M., Dincer, I and Javani, N. 2019. Thermodynamic modeling of a solar energy based combined cycle with rock bed heat storage system, *Solar Energy*, In Press: https://doi.org/10.1016/j.solener.2019.03.053.

Pietsch, A. and Brandes, D.J., 1989. Advanced solar Brayton space power systems, Proceedings of Intersociety Energy Conversion Engineering Conference (IECEC), Los Alamitos (CA).

Shah, R.K., 2005. Compact Heat Exchangers for Microturbines, Proceedings of Fifth International Conference on Enhanced, Compact and Ultra-Compact Heat Exchangers: Science, Engineering and Technology (CHE2005 – 31), Hoboken, USA, September.

Shiraishi, K. and Ono, Y., 2007. Hybrid turbocharger with integrated high speed motor-generator. Mitsubishi Heavy Industries, Ltd. Technical Review 44(1).

Snyman, J.A., 2009. Practical mathematical optimization, Pretoria: University of Pretoria.

Stine, B.S. and Harrigan, R.W., 1985. Solar energy fundamentals and design. New York: John Wiley & Sons, Inc.

Visser, W.P.J., Shakariyants, S.A. and Oostveen, M., 2011. Development of a 3 kW microturbine for CHP applications. *Journal of Engineering for Gas Turbines and Power* 133, pp. 042301:1-8.

Wang, W., Laumert, B., Xu, H. and Strand, T., 2015. Conjugate heat transfer analysis of an impinging receiver design for a dish-Brayton system. *Solar Energy* 119, pp. 298-309.

Wahlström, J. and Eriksson, L., 2011. Modeling diesel engines with a variable-geometry turbocharger and exhaust gas recirculation by optimization of model parameters for capturing non-linear system dynamics. Proceedings of the Institution of Mechanical Engineers, Part D, Journal of Automobile Engineering 225 (July 7).

Westin, F., 2005. Simulation of turbocharged SI-engines–with focus on the turbine. Doctoral thesis. KTH School of Industrial Engineering and Management, TRITA–MMK 2005:05. Stockholm: Royal Institute of Technology.

Willis, H.L. and Scott, W.G., 2000. Distributed power generation, CRC Press: New York.

Wilson, D.G. and Korakianitis T., 1998. The design of high-efficiency turbomachinery and gas turbines, 2nd ed. New Jersey: Prentice Hall.

Withey, E., Kruizenga, A., Andraka, C. and Gibbs, P., 2016. Plasma sprayed coatings for containment of Cu-Mg-Si metallic phase change material. *Surface & Coatings Technology* 304, pp. 117–124.

Yan, M. and Fan, Z., 2001. Durability of materials in molten aluminum alloys. *Journal of Material Science* 36, pp. 298-295.